Incident Wavelength Resolved Resonant SERS on Au Sphere Segment Void (SSV) Arrays

Nicolás G. Tognalli,*,[†] Alejandro Fainstein,[†] Ernesto J. Calvo,[‡] Mamdouh Abdelsalam,[§] and Philip N. Bartlett[§]

[†]Centro Atómico Bariloche and Instituto Balseiro, Comisión Nacional de Energía Atómica, 8400 S. C. de Bariloche, Río Negro, Argentina

[‡]Electrochemistry Group, INQUIMAE FCEyN, Pabellon 2, Ciudad Universitaria, AR-1428 Buenos Aires, Argentina

[§]School of Chemistry, University of Southampton, Southampton, SO17 1BJ, United Kingdom

ABSTRACT: Sphere segment void (SSV) arrays allow the reproducible engineering of plasmon-polariton modes from the near-infrared to the ultraviolet through the tuning of the void height and diameter. The wavelength dependence of surface-enhanced Raman scattering (SERS) can then in principle be controlled by selecting these parameters. Using 4-mercaptopyridine as a covalently bonded nonresonant molecular probe, we report a detailed study of such wavelength dependence of SERS in Au SSV arrays as a function of void diameter and height. We conclude that the SERS mechanism on SSV arrays depends on the plasmonic properties of the substrates and also that additional effects contribute significantly to the observed enhancement including a chemical contribution related to the molecular probe and a nanostructuring induced surface plasmon localization existent for the smaller cavity dimensions.
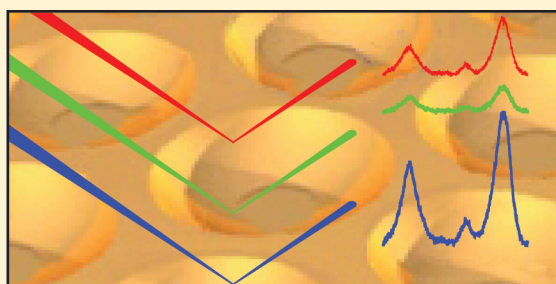
I. INTRODUCTION

In the past decade, there have been important efforts in developing appropriate substrates for surface-enhanced Raman scattering (SERS).[1−7] The driving force behind this research is related to the fundamental understanding of the SERS process and also to the measurement of molecular concentrations with high sensitivity, specificity, and analytical precision.[8] A substrate may perform well for one of these purposes but not for the others. Typically, substrates with higher SERS amplification display lower reproducibility and control of the significant parameters.[9,10] Conversely, substrates with better controlled and reproducible performance may present a smaller but still significant amplifying factor.[4,5,7] For both analytical applications and research on the SERS principles, the latter is particularly attractive. Sphere segment void (SSV) arrays are one of these kinds of substrates developed a few years ago and actively studied in their plasmon-polariton properties.[11−22] These substrates, with reported SERS enhancements in the $10^5−10^7$ range, are reproducible, highly homogeneous, and stable, and they present a large series of parameters that can be experimentally controlled to adapt the plasmon-polariton response to specific aims.[18,19] They can, in addition, be combined with metallic nanoparticles to provide SERS enhancements reportedly larger than those of nanoparticle dimers.[23−25]

Notwithstanding these notable advantages and potentialities, it turns out that a clear direct and general demonstration of the correlation between engineered plasmon energies and wavelength-dependent SERS enhancement in SSV arrays is still lacking with several partial reports suggesting a nontrivial relation between the two.[15,18−22] Several phenomena may contribute to this complexity, including molecular electronic resonances of the chosen analytes, metal-molecule electronic transitions of chemically adsorbed species, incoming combined with outgoing Raman resonances, and the nanostructuring of the crownlike cavity features usually not taken into account in the theoretical models and not leading to narrow plasmon resonances. In addition, from the experimental point of view, all the reported investigations have relied on single-channel Raman spectrometers with access to only a few discrete number of laser wavelengths thus providing only a limited perspective to the problem under consideration. To address these issues in this article, we present a detailed resonant study of the SERS wavelength response of Au nanocavity arrays as a function of void diameter and height. This investigation has been performed with a triple-spectrometer and with access to almost continuable tunable laser wavelengths in the spectral region relevant to the studied substrates. As a molecular probe, we use a monolayer of covalently bonded 4-mercaptopyridine molecules that, in solution, do not possess electronic resonances in the visible near-infrared (NIR) range. We show that indeed the dispersion of the Bragg and Mie-like cavity plasmons is not sufficient by itself to describe the observed dependence of SERS enhancement with laser energy, and we

discuss the possible mechanisms leading to these observations. This resonance study is relevant to determine optimal experimental condition for SERS applications of the SSV arrays, including the tuning of the substrate response to optimize the detection capability of electronically resonant and nonresonant molecular analytes.

Metallic nanocavity arrays have been developed by Bartlett et al.[11] These nanostructures present two different types of surface plasmon polaritons (SPPs): Mie or localized SPPs (LSPPs) and Bragg or propagating SPPs (PSPPs). The former are related to the electromagnetic solution to the problem of light scattered by a dielectric sphere with size (radius = a) comparable to the wavelength of light ($2\pi/k$) usually referred to as Mie scattering.[26] An illustrative starting point is that of a spherical void surrounded by an infinite metallic medium, a kind of antinanoparticle.[12] For small spheres ($ka \ll 1$), the quasi-static solution for this model problem gives the following LSSP resonance frequency ω_l as a function of the angular momentum l:

$$\omega_l = \omega_{sp}\sqrt{(l+1)/(2l+1)} \tag{1}$$

where ω_{sp} is the 2D surface plasmon frequency. The field distributions of the plasmon-polariton modes inside the cavity follow the symmetry of the $Y_{(l-1,m)}$ spherical harmonics, and they are more confined to the metallic surface as l increases. Moreover, there are also $2l + 1$ LSPP states with the same degenerate energy because of the different angular projections ($-l \leq m \leq l$). If the cavity is truncated, the loss of symmetry splits the level into $2l + 1$ states.[15,20] On the other hand, if the cavity radius is close to the wavelength of light ($1 \sim ka$), retardation effects appear modifying the plasmon-polariton frequency showed in eq 1. These LSPPs combine the properties of Mie plasmons of a metallic void with those of the whispering gallery modes of an optical cavity.[14] This combined behavior cannot be separated, and thus computational calculations are needed to determine the Mie mode energies. The Mie modes are usually labeled according to their angular moment l and projection m upon the substrate normal axis using an atomic physics convention, $^m l$, where S corresponds to $l = 0$, P to $l = 1$, D to $l = 2$, and F to $l = 3$, and the supraindex refers to the projection m.

The second kind of surface plasmon-polaritons, the PSPPs, appear when there is a rupture of the full translational invariance of a metallic surface caused by a periodic corrugation, a grating. This allows light to couple to propagating surface plasmon polaritons by providing the former an in-plane momentum $q_{m,n} = 2\pi/\lambda_{m,n}$, where $\lambda_{m,n} = C(m\mathbf{a} + n\mathbf{b})$ is a distance between scatter planes in the reciprocal space of the grating, C is a constant depending of the geometry, $\mathbf{a}$ and $\mathbf{b}$ are the reciprocal unit vectors, and m and n are integers.[14,27] Therefore, the excitation of these plasmons depends on the surface grating, in this case a hexagonal array of cavities acting as a periodical dispersion potential; on the light wavelength and polarization; and on both its polar and azimuthal incidence angles.[14,16]

During recent years, there has been important theoretical work developed to understand the optical properties of these metallic nanocavity arrays, in particular, to reproduce and to predict the SPPs probed through optical reflectivity measurements.[13−16] There have been also different experimental investigations to explore and to understand the physical properties of these systems: the determination of the spatial field distribution of the SPPs using scanning near-field optical microscopy (SNOM),[17] the analysis of the angle-resolved Raman scattering response,[18] studies on the SERS enhancement factor,[19] correlation between SERS intensity and plasmon modes,[20] and also studies on electromagnetic versus chemical SERS contributions on these SSV arrays.[21] Finally, some of the applications of these nanostructured metallic SERS platforms were related to analyze the response of different redox molecules under in situ electrochemical experiments[28] and mutations in DNA sequences[29] and also to amplify the Raman signal coming from optical responsive glucose nanosensors.[23,24]

In this report, we focus our efforts to study in a detailed way the possibility to use these SSV arrays as a surface-enhanced resonant Raman scattering (SERRS) platform. For this purpose, it is essential to clearly determine the role and spectral dependence of the different enhancement mechanisms active in these substrates. We present an incidence wavelength resolved SERS study over a wide range of plasmon-polariton responses coming from gold nanocavity arrays with different void diameters (d) and heights ($0 < h = t/d < 1$, where t is the cavity thickness). We evidence that tuning to SPPs is indeed needed to get SERS signals from the self-assembled molecule. The SERS response is correlated to the SPP mode energy dispersion that arises with changes on the void diameter and height. Nevertheless, we will show that this correlation is a complex one with additional contributions due to chemical mechanisms and possibly surface nanostructuring (in the case of the smaller diameter cavities) being needed to fully describe the observed behavior.

The article is organized as follows. We begin with an Experimental Section, where we describe the fabrication procedure and the Raman and reflectivity measurement conditions. In the Results and Discussion section, reflectivity and Raman measurements are then presented and discussed as a function of the cavity diameter, height, and laser excitation wavelength. Finally, Conclusions are drawn.

II. EXPERIMENTAL SECTION

The nanovoid arrays are fabricated via a hexagonal close-packed self-assembly of polystyrene spheres (Duke Scientific Corporation) with diameters ranging from 500 to 800 nm followed by an electrochemical Au deposition (TG-25 RTU, Technic Inc.).[11] During this process, the 1% water solution of nanospheres fills a thin cell made of a cysteamine modified gold-coated glass slide (AU.1000.ALSI, Platypus Technologies), a clean glass slide, and sidewalls made of a 300 μm thick spacer of Parafilm. The cysteamine monolayer is incorporated to help fill the thin cell and to reduce the contact angle of the aqueous solution on the surface. This forms a sweeping meniscus tail as the fluid dries, which pulls spheres to the evaporation line where they form a close-packed monolayer domain. After the self-assembly of the polystyrene template, the sample is immersed into the electrochemical plating bath. By controlling the deposition rate and time, the cavity height can be determined. Moreover, by systematically retracting the sample every 500 μm from the electrochemical bath during the metal deposition, it is possible to achieve different cavity heights in one single graded sample. Finally, the sample is sonicated in dimethylformamide (DMF) to remove the polystyrene template. As a result, very clean, reproducible, and well-defined hexagonal arrays of Au nanocavities with diameters between 500 and 800 nm are obtained over areas of ~1 cm^2. In Figure 1, we present typical scanning electron
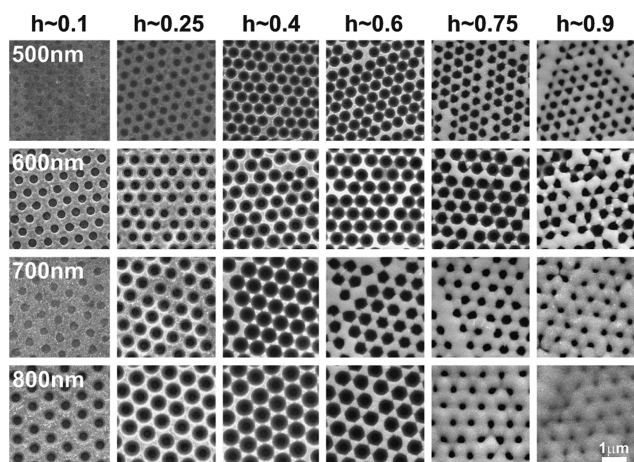
Figure 1. SEM images of four graded Au nanocavity arrays with different void diameters between 500 and 800 nm (indicated inside the first picture of each line). The cavity heights grow from left to right along each line starting from $h \sim 0.1$ to $h \sim 0.9$.

microscope (SEM) images acquired over the studied graded Au nanocavity array samples with 500, 600, 700, and 800 nm void diameters (from top to bottom) and cavity heights between $h \sim 0.1$ and $h \sim 0.9$ (from left to right). We will refer to these graded gold cavity substrates as Au500g, Au600g, Au700g, and Au800g according to their void diameter.

The reflectivity measurements were performed using a fully automated Wollam WVASE32 variable angle spectroscopic ellipsometer with focusing probes that give a 100 μm circular spot on the sample sustaining a numerical aperture of $\sim$0.02. The experiments were performed using P-polarized light between 400 and 1000 nm every 5 nm at 25° incidence angle referred with respect to the normal to the sample surface. The $X-Y$ sample stage is also automated so we can acquire the reflectivities along the different graded steps on a sample in a single programmed scan.

For the resonant Raman scattering experiments, we used a Jobin-Yvon T64000 triple spectrometer operating in subtractive mode and equipped with a liquid N_2 cooled charge-coupled device (CCD). The excitation was done using the 647.1 and 676.1 nm lines of an Ar−Kr laser and a continuously tunable Ti-Sapph laser between 690 and 850 nm. We performed the acquisitions for 10 s using 20mW laser power focused with a numerical aperture of $\sim$0.02 on a circular spot of $\sim$30 μm diameter with an incident angle of 15°.[30] The spot position on the sample was manually controlled, and the Raman measurements were collected in a backscattering configuration with a $\sim$0.25 numerical aperture lens. All presented spectral intensities were corrected for the ω^4 energy dependence and the spectrometer response.

To accomplish the resonant SERS measurements, a self-assembled monolayer of 4-mercatopyridine (4MP) was grown by immersing the SSV arrays into a 10 mM ethanolic solution of this molecule for 30 min and then by rinsing with ethanol and finally by drying with a nitrogen gas flow. We chose 4MP because it is a molecule that does not present optical absorptions in the visible-NIR range when it is in solution (the lowest energy absorption is centered at 320 nm in the UV).[21] We have recently demonstrated, however, that a resonant molecule-to-metal transition is available around 670 nm when 4MP is self-assembled on Au and Ag substrates.[21] As

a result, both electromagnetic and chemical contribution to SERS in SSV arrays are relevant in these experiments.

III. RESULTS AND DISCUSSION

To introduce the different surface plasmon polaritons (SPPs) of sphere segment void (SSV) arrays, we begin by presenting in Figure 2 typical optical reflectivity curves measured on a graded
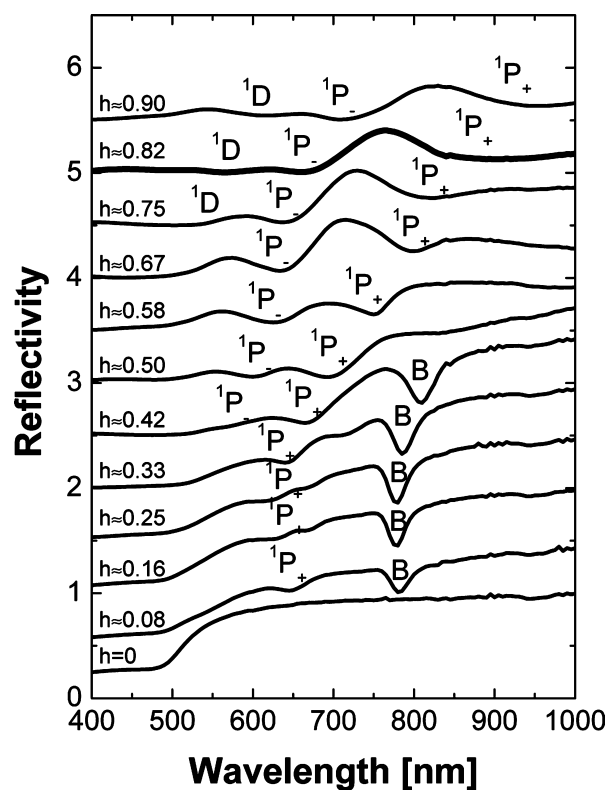

Figure 2. Optical reflectivities measured with P-polarized light between 400 and 1000 nm every 5 nm at 25° incidence angle on a graded Au SSV array with 600 nm void diameter. Each reflectivity curve corresponds to a measurement performed on a different cavity height ranging between $h = 0$ (flat Au) and $h \sim 0.9$ (full cavities) from bottom to top. Curves are vertically shifted in 0.5 respect to the previous one for clarity purposes. Dips indicate the presence of surface plasmon polaritons denoted as B, $^1P_+$, $^1P_-$, and ^1D which refer to a Bragg and three different Mie modes (see text for details).

Au SSV sample with 600 nm void diameter. Each reflectivity curve corresponds to a measurement performed on a different cavity height, h, ranging from bottom to top between $h = 0$ (flat Au) and $h \sim 0.9$ (full cavities) through almost equal steps. Curves are vertically shifted in 0.5 respect to the previous one for clarity purposes. We have not observed differences in the reflectivities measured with and without the self-assembled molecular probe.[21] The flat Au ($h = 0$) presents a reflectivity $R \sim 1$ above 600 nm that falls for smaller wavelengths because of the Au interband electronic transitions.[27] On the other hand, dips in the other reflectivity curves indicate the presence of SPP modes, while the diffraction effects can be neglected according to ref 14. Following the accepted labeling of these modes,[14,15,18,20] we assign the one denoted as B to the $q_{\overline{11}}$ Bragg mode.[31] For a given lattice parameter (or cavity diameter d), Bragg modes present well-defined energies and angular dispersions. Energy and in-plane momentum conservation laws define the incidence angle and wavelength required for their

excitation. Bragg modes only appear when a flat surface between cavities is accessible for propagation mode ($h < 0.3$ or $0.75 < h$).[14] In Figure 2, we observe the $q_{\overline{11}}$ Bragg mode only for $h < 0.3$.

The absence of the Bragg mode in the $0.75 < h$ region is presumably due to the nanostructuring of the surface occurring for small diameter nanocavity substrates as reported in ref 22. Such nanostructuring can be observed in Figure 1 and in additional higher resolution images we have performed on this series of samples (not shown). Bragg modes should not disperse as a function of cavity thickness if no plasmon interactions are present in the substrate. That is not the case in SSV arrays because of the presence of Mie modes[13] that induce dispersion of the B modes as a function of h as can be observed in Figure 2. On the other hand, dips denoted as $^1P_+$, $^1P_-$, and ^1D are assigned to the different Mie modes presented in the Introduction. This assignment is in good agreement with theoretical and experimental results presented in refs 14 and 20. Modes $^1P_+$ and $^1P_-$ are the bonding and antibonding states resulting from the coupling between the ^1P pure dipolar Mie mode and the cavity rim mode, a dipolar LSPP arising in the region where the void matches the planar region of the SSV.[15] The ^1D mode refers to the quadrupole Mie mode with projection $m = 1$.[14,15,18] Mie modes change their energies as a function of h as can be observed in Figure 2 and also as a function of d as will be presented later. These variations are due to changes in the field confinement boundary conditions. Finally, we note that Mie modes do not disperse as a function of light incidence angle. Because of the symmetry of the voids, however, different angular projections of the Mie modes (m values) are excited as a function of incidence angle depending on the overlap of the LSPP and light fields.[15]

In Figure 3, we present typical Raman spectra of 4MP self-assembled on the Au600g sample at $h \sim 0.82$ corresponding to the reflectivity curve highlighted with a thicker line in Figure 2 measured as a function of laser wavelength (indicated in each spectrum). Peaks centered at 1004, 1064, 1097, and 1208 cm^{-1} are related to C−C stretching, C−H bending, C−C stretching, and C−H and N−H bending, respectively.[32] It can be observed how the Raman intensity changes as the laser wavelength varies. In particular, there is a first maximum around 650−670 nm[21] that falls into a minimum as the laser wavelength goes through 750 nm and finally rises again to reach a second maximum around 790−830 nm. This wavelength dependence of the Raman intensity can be interpreted as because of a laser resonant tunning with the plasmon modes corresponding to the $^1P_-$ and $^1P_+$ excitations as displayed by the highlighted reflectivity of Figure 2 (thicker curve). In addition, there is a difference between the magnitude of the two observed intensity maxima. This behavior, as it will become clearer in the following discussion, reflects two contributions. The first, as was mentioned in the Experimental Section, is due to the Au-4MP molecule-to-metal charge-transfer chemical resonance around 670 nm.[21] The second could be related to the different field distributions arising from the $^1P_+$ and $^1P_-$ Mie modes and their corresponding SERS efficiency as was discussed in refs 15 and 20.

To identify and characterize both the electromagnetic and the chemical contributions to SERS in these plasmonic SSV arrays, we present in Figure 4 a comparative and systematic study of the reflectivity and Raman intensity as a function of incidence wavelength and SSV height and diameter on the four graded cavity samples: Au500g, Au600g, Au700g, and Au800g
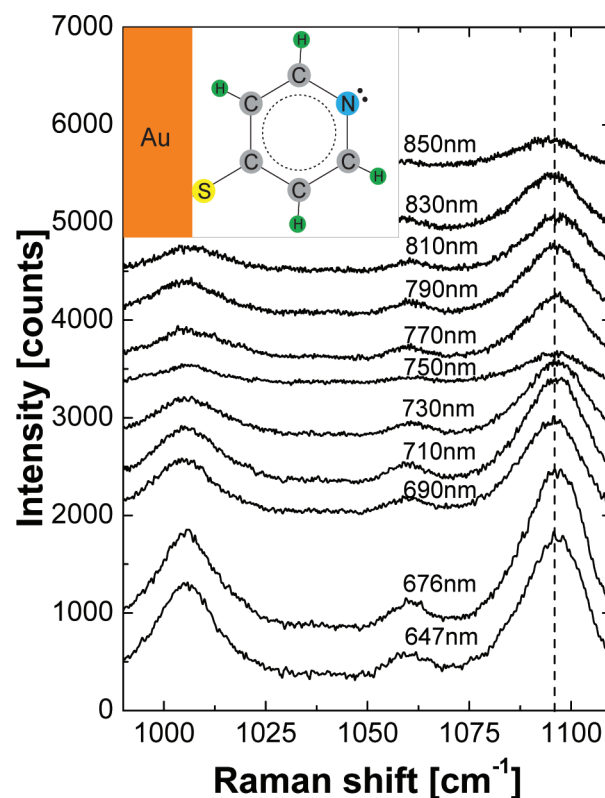

Figure 3. Raman spectra of 4MP self-assembled on the Au600g sample at $h \sim 0.82$ measured as a function of laser wavelength (indicated in each spectrum). Spectra are raw data, and they are vertically shifted for clarity. Peaks centered at 1004, 1064, 1097, and 1208 cm^{-1} are related to C−C stretching, C−H bending, C−C stretching, and C−H and N−H bending, respectively.[32] The inset presents a scheme of the self-assembled 4MP.

(graphs from top to bottom). In the left panel of Figure 4, we show optical reflectivities like those presented in Figure 2 as a function of λ, h, and d. The data corresponding to Au600g and presented in Figure 2 are repeated in Figure 4 for ease of comparison with the Raman intensity profiles. As in Figure 2, dips in the reflectivity curves indicate the presence of different surface plasmon polaritons denoted as B, $^1P_+$, $^1P_-$, ^1D, and ^1F which refer to the $q_{\overline{11}}$ Bragg mode, the bonding and antibonding dipolar Mie modes, and the $m = 1$ projection of the $l = 2$ and $l = 3$ Mie modes, respectively. All the plasmon modes observed here are in good agreement with previously reported theoretical and experimental results as a function of the different parameters.[13−15,20]

As expected, the $q_{\overline{11}}$ Bragg mode increase its wavelength as d increases.[14] This is because an increment on the cavity diameter d implies an increase on the lattice parameter of the void hexagonal structure. This leads to a decrease on the reciprocal lattice parameter or, equivalently, of the first Brillouin zone length. Consequently, the Bragg SPP, which in the studied samples always corresponds to the $q_{\overline{11}}$ reciprocal wavevector folded to the center of the first Brillouin zone, decreases its energy as d increases. All Bragg modes display a dispersion with increasing h because of the interaction with the Mie modes also present in the SSV arrays. As discussed above, these Bragg modes appear always for $h < 0.3$ in the four studied substrates. In addition, they can also be observed for $0.75 < h$ in the Au700g and Au800g samples. This last fact is related to the quality of the grown samples. As follows from detailed SEM
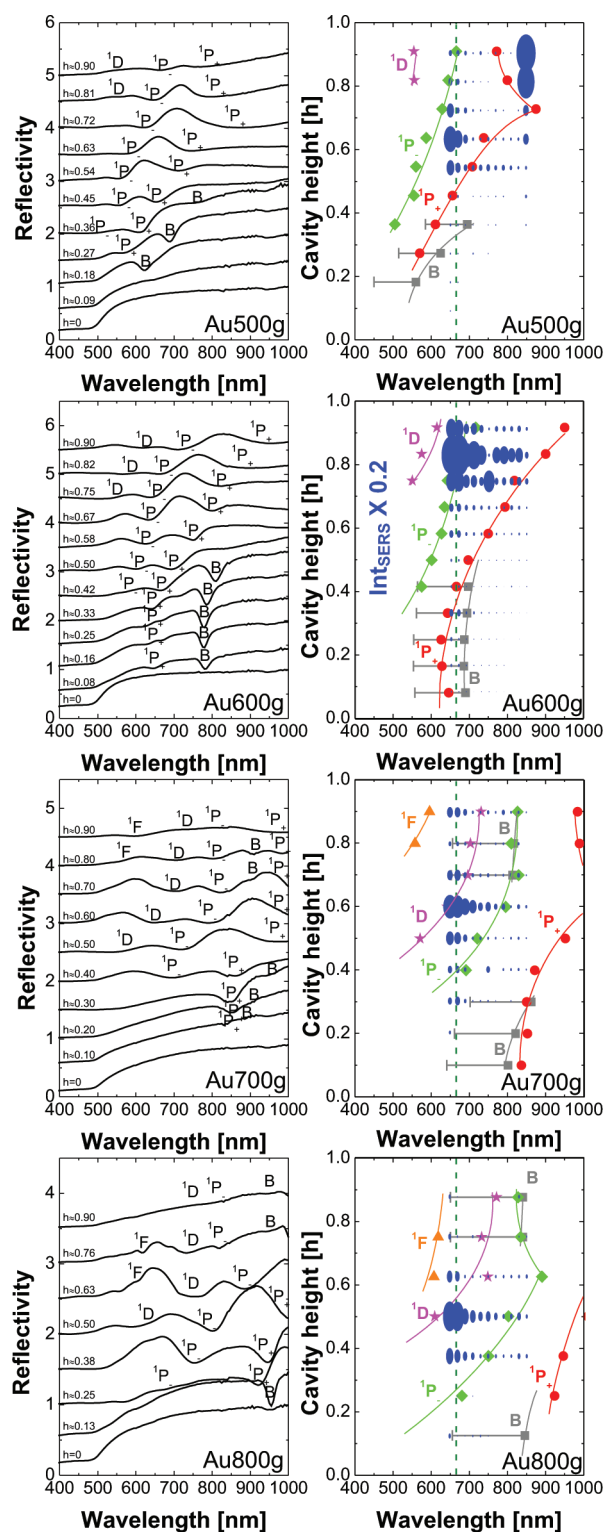
Figure 4. Left panel: Optical reflectivities as presented in Figure 2 for SSV arrays with diameters 500, 600, 700, and 800 nm (from top to bottom). Dips are assigned to different SPP modes as introduced in the text. Right panel: Plasmon modes based on the curves shown in the left panel. The squares, circles, diamonds, stars, and triangles indicate the measured position of the Bragg and Mie $^1P_+$, $^1P_-$, ^1D, and ^1F SPPs, respectively. The full lines are guides to the eye. Bragg modes have been corrected for the angle differences between reflectivity (25°) and Raman (15°) setups. The gray horizontal bars indicate the available energies for the Bragg modes inside the Raman experimental collection angle. The bubble map presents the Raman intensity

Figure 4. continued

measured at each specific laser wavelength and cavity height where the bubble is centered. The size of the bubbles is linearly proportional to the measured SERS intensity of the 4MP 1097 cm^{-1} peak (except for Au600g for which the intensities have been divided by 5). The vertical dashed lines indicate the position of the Au-4MP charge-transfer resonance studied and described in ref 21.

images (see, e.g., Figure 1), these two SSV arrays present smoother and more continuous surfaces between voids for 0.75 < h as is required for the Bragg modes to propagate. Turning now to the Mie modes, they also shift to larger wavelengths as the cavity diameters increase along the set of samples (from top to bottom in Figure 4). In this case, the phenomenon is related to the electromagnetic field confinement, that is, as the void diameter increases the same occurs with the confined wavelength. It is also noticeable that as the angular number l increases the LSPP modes shift to higher energies as expected from eq 1. Finally, the $^1P_+$, $^1P_-$, ^1D, and ^1F Mie SPPs disperse to smaller wavelengths as h decreases. This reflects the stress on the plasmon-polariton confinement caused by a larger truncation of the cavities and the corresponding lose of the spherical symmetry.[15]

To study the resonant SERS response of these nanostructured substrates, a molecular probe is required. The 4MP was chosen essentially for two reasons: First, it forms homogeneous, reproducible, and self-limited monolayer coverages of covalently bound molecules. Second, it does not contribute with molecular electronic resonances to the Raman cross section since its lower energy optical transition is in the UV at ~320 nm. It turns out, however, that when bound to a metal a new charge-transfer transition connecting the molecule (in this case, the highest occupied molecular orbital (HOMO) state) and the Fermi level appears that contributes to the Raman resonant enhancement.[21] For 4MP, it has been determined that this latter transition contributing to the so-called chemical enhancement occurs at 670 nm.[21] Far from being specific to 4MP, we emphasize that this is a general feature that has to be considered when molecules are chemically adsorbed in a substrate, which is an effect that can be studied in the substrates described here.

In the right panel of Figure 4, we present the plasmonic maps on the basis of the curves shown in the left panel of the same figure. The squares, circles, diamonds, stars, and triangles indicate the measured position of the Bragg and Mie $^1P_+$, $^1P_-$, ^1D, and ^1F SPPs, respectively, also taken from the corresponding graphs of the left panel.[30] The full lines are guides to the eye. The Bragg mode wavelengths have been corrected for the angle differences between reflectivity (25°) and Raman (15°) measurement setups. The gray bars indicate the available energies for the Bragg modes within the Raman experimental collection angle. We have also indicated with a vertical dashed line the spectral position for the charge-transfer HOMO-to-Fermi level resonance in Au-4MP studied and described in ref 21. Finally, we superimpose in each graph a bubble map where the size of each bubble is linearly proportional to the SERS intensity measured at the specific cavity height and with the corresponding laser wavelength where the h and λ coordinates of that bubble are centered. The intensities displayed correspond to the amplitude of the 4MP 1097 cm^{-1} peak indicated with a dashed line in Figure 3. The intensity scales are the same for all the bubble maps except for

that corresponding to the Au600g sample which has been divided by a factor of 5 as indicated in the corresponding panel. We recall that the Raman intensities are already corrected for both the ω^4 and the spectrometer responses. These Raman data were measured varying λ by 20 nm steps between 650 nm and 850 nm with two accumulations of 10 s each using P-polarized light and a laser power of 20 mW focused on a circular spot of $\sim$30 μm in diameter. Each map presents the result of $\sim$100 Raman measurements performed varying the cavity height in steps of $\Delta h \sim 0.1$ by moving the spot position in 500 μm steps along the graded sample.

It follows from the results presented in Figure 4 that the correlation between maximum SERS enhancement and plasmon energies is not straightforward. In what follows, we will discuss conclusions that can be drawn from these results and possible explanations for the observed effects. First, the maximum SERS intensity from all samples is comparable with only a modest larger amplification observed for the Au600g SSV array where the maximum on the Raman signal is $\sim$10 times larger than that obtained for the rest of the substrates. This homogeneity between substrates can be taken as additional proof of growth control and predictable responses in this kind of SSV substrates. Second, the absolute Raman maximum for the four samples falls around 650−670 nm, that is, at the Au-4MP molecule-to-metal charge-transfer resonance independently of the underlying plasmonic response of each substrate. This is an important result that confirms that the chemical contribution to SERS is present in these systems with the HOMO-to-Fermi level transition providing significant electronic enhancement to the Raman cross section. It also implies that even when optical absorption is not present in the free molecular probe, the situation where the probe is bound to the metal has to be specifically analyzed. Third, while this proves that the chemical contribution to SERS cannot be neglected a priori to fully understand the SERS response, we emphasize that Raman signals have not been detected in flat Au-substrates modified with 4MP. Thus, it is clear that it is the combination of metal-surface-induced electronic resonances and plasmon excitation that is critical to the observed signals. Fourth, and pointing our attention now to the electromagnetic contribution to the SERS mechanism, we conclude from these maps that there exists a correlation between more intense Raman signals and the crossing between the energies defined by the HOMO-to-Fermi level transition and the ^1D-like Mie plasmon states. This is particularly clear for the cavities with diameters in the range 600−800 nm and is not present only for the Au500g substrate for which the ^1D-like states fall in the small wavelength region where plasmons in Au are quenched by absorption. As follows from calculations of plasmon modes in truncated metallic cavities, ^1D Mie states present a field distribution with maximum intensity close to the void surface, where the probe molecules are self-assembled. Conversely, ^1P-like modes lead to field intensities mainly concentrated in the void center and away from the molecule.[25] We can hence conclude that the field distribution of the plasmon modes and the spatial position of the probe are very important to take advantage of the maximum SERS amplification of the SSV arrays.

We note from Figure 4 that there is evidence that an additional mechanism is coming into play for the substrates with smaller void diameters (Au500g and Au600g) and with larger substrate thicknesses ($h > 0.5$). Indeed, the largest amplification is observed for the Au600g substrate at large h in a spectral region where both ^1D and $^1P_-$ states are present. Moreover, significant enhancement associated to the ^1P states is observable for the Au500g substrate in this thickness range, where cavities begin to close and crownlike cusps develop at the surface. Such enhancement related to ^1P-like plasmon states was not observable for the larger diameter cavities (Au700g and Au800g). To provide a possible explanation for this observation, we comment here about recent results of selective molecular decoration of nanoncavity arrays,[22] which demonstrated that significantly greater Raman signals are observed when the molecules are located at the top surface of the array as compared with the cavity walls. This behavior was observed for $h = 0.8$ and was more relevant as the cavity dimensions decreased. The proposed explanation was related to the localization of surface modes induced by the nanostructuring of the surfaces (as opposed to more extended Bragg-like behavior in larger-diameter cavities), which leads to a localization and, hence, enhancement of the local electromagnetic fields. Such results are compatible with the Raman enhancement we have observed. In addition, our detailed wavelength dependent reflectivity and Raman investigation provides additional support for this interpretation basically for three important reasons. Namely, (1) we have observed a poor Raman enhancement related to the tunning of extended Bragg-like B-modes as compared to that obtained with Mie SPPs resonances on the four studied samples (see the size of the bubbles along the gray bars in Figure 4);[33] (2) while for the larger diameter void substrates Bragg-like B-modes have been detected at large thicknesses (see the left planels related to Au700g and Au800g in Figure 4), no similar observations appear for the smaller cavity systems (Au500g and Au600g) providing further proof of plasmon localization in these latter structures; and (3) the larger enhancement related to these surface-localized modes is observed close to the two ^1P-like states that, according to the literature, are relevant to couple far-field light with the rimlike modes which are closely connected to the top surface crownlike features and surface imperfections.[15]

IV. CONCLUSIONS

We performed a detailed study of the combined plasmonic properties and Raman wavelength enhancement dependence of well-ordered Au SSV arrays for void diameters between 500 and 800 nm. The laser wavelength was varied continuously in the relevant spectral region between 650 and 850 nm on structures with controlled thickness/diameter ratio (h) in the range $0 \leq h \leq 1$. In agreement with previous investigations, we verified the presence of two types of surface plasmon-polaritons: propagating (or Bragg) and localized (or Mie). As expected, Bragg modes are always observed for shallow cavities ($h < 0.3$). We found, in addition, that in the studied structures a reappearance of these modes is verified for $0.75 < h$ at the largest void sizes 700 and 800 nm. For these structures, the surface between voids is well-defined. Conversely, B-like modes are not observed at large h for the smaller diameter cavities signaling the possibility of nanostructuring induced plasmon localization. Different Mie modes of P, D, and F-like character are evidenced for $\sim$0.2 $< h$. Self-assembled 4MP was used as a molecular probe because of its surface homogeneity and lack of pure molecule-related electronic resonant transitions in the visible and NIR range.

The results presented demonstrate that the resonant Raman response of the substrates is quite complex involving not only

the coupling to the cavity-void specific plasmon modes but also being determined by contributions due to molecule-to-metal charge-transfer transitions and coupling to surface-localized plasmon modes of the smaller diameter structures. The main conclusions can be summarized as follows: (1) there is a tuning of the Raman enhancement to metal-molecule charge-transfer transitions that are specific to the covalently bound molecule under study, (2) coupling to surface plasmons is nevertheless critical for enhanced Raman signals with ^1D-like plasmon modes being more efficient than the ^1P-like ones. This is presumably due to their associated field localized closer to the surface. (3) Propagating Bragg-like plasmon modes are inefficient to provide significant Raman enhancement, and (4) for small diameter voids and large h, an additional coupling to localized plasmon states, mediated by the laser coupling to ^1P-like modes, may be providing an additional strong channel of Raman amplification in these ordered cavity metallic substrates.

■ AUTHOR INFORMATION

Corresponding Author

*E-mail: tognalli@cab.cnea.gov.ar.

Notes

The authors declare no competing financial interest.

■ ACKNOWLEDGMENTS

■ REFERENCES

(1) Etchegoin, P.; Maher, R. C.; Cohen, L. F.; Hartigan, H.; Brown, R. J. C.; Milton, M. J. T.; Gallop, J. C. *Chem. Phys. Lett.* **2003**, *375*, 84−90.

(2) Freeman, R. G.; Grabar, K. C.; Allison, K. J.; Bright, R. M.; Davis, J. A.; Guthrie, A. P.; Hommer, M. B.; Jackson, M. A.; Smith, P. C.; Walter, D. G.; Natan, M. J. *Science* **1995**, *267*, 1629−1632.

(3) Kiely, C. J.; Fink, J.; Brust, M.; Bethell, D.; Schiffrin, D. J. *Nature* **1998**, *396*, 444−446.

(4) Félidj, N.; Aubard, J.; Lévi, G.; Krenn, J. R.; Salerno, M.; Schider, G.; Lamprecht, B.; Leitner, A.; Aussenegg, F. R. *Phys. Rev. B* **2002**, *65*, 075419−1/9.

(5) Jackson, J. B.; Westcott, S. L.; Hirsch, L. R.; West, J. L.; Halas, N. J. *Appl. Phys. Lett.* **2003**, *82*, 257−259.

(6) Kelly, K. L.; Coronado, E.; Zhao, L. L.; Schatz, G. C. *J. Phys. Chem. B* **2003**, *107*, 668−677.

(7) Dick, L. A.; McFarland, A. D.; Haynes, C. L.; Van Duyne, R. P. *J. Phys. Chem. B* **2002**, *106*, 853−860.

(8) Le Ru, E. C.; Meyer, M.; Etchegoin, P. *J. Phys. Chem. B* **2006**, *110*, 1944−1948.

(9) Maher, R. C.; Cohen, L. F.; Etchegoin, P. *Chem. Phys. Lett.* **2002**, *352*, 378−384.

(10) Tognalli, N.; Fainstein, A.; Calvo, E.; Bonazzola, C.; Pietrasanta, L.; Campoy-Quiles, M.; Etchegoin, P. *J. Chem. Phys.* **2005**, *123*, 044707−1/9.

(11) Bartlett, P. N.; Birkin, P. R.; Ghanem, M. A. *Chem. Commun.* **2000**, 1671−1672.

(12) Coyle, S.; Netti, M. C.; Baumberg, J. J.; Ghanem, M. A.; Birkin, P. R.; Bartlett, P. N.; Whittaker, D. M. *Phys. Rev. Lett.* **2001**, *87*, 176801−1/4.

(13) Kelf, T. A.; Sugawara, Y.; Baumberg, J. J.; Abdelsalam, M. E.; Bartlett, P. N. *Phys. Rev. Lett.* **2005**, *95*, 116802−1/4.

(14) Kelf, T. A.; Sugawara, Y.; Cole, R. M.; Baumberg, J. J.; Abdelsalam, M. E.; Cintra, S.; Mahajan, S.; Russell, A. E.; Bartlett, P. N. *Phys. Rev. B* **2006**, *74*, 245415−1/12.

(15) Cole, R. M.; Baumberg, J. J.; García de Abajo, F. J.; Mahajan, S.; Abdelsalam, M. E.; Bartlett, P. N. *Nano Lett.* **2007**, *7*, 2094−2100.

(16) Teperik, T. V.; Popov, V. V.; García de Abajo, F. J.; Abdelsalam, M.; Bartlett, P. N.; Kelf, T. A.; Sugawara, Y.; Baumberg, J. J. *Opt. Express* **2006**, *14*, 1965−1972.

(17) Lacharmoise, P. D.; Tognalli, N. G.; Goñi, A. R.; Alonso, M. I.; Fainstein, A.; Cole, R. M.; Baumberg, J. J.; García de Abajo, F. J.; Bartlett, P. N. *Phys. Rev. B* **2008**, *78*, 125410−1/5.

(18) Baumberg, J. J.; Kelf, T. A.; Sugawara, Y.; Cintra, S.; Abdelsalam, M. E.; Bartlett, P. N.; Russell, A. *Nano Lett.* **2005**, *5*, 2262−2267.

(19) Cintra, S. H.; Abdelsalam, M. E.; Bartlett, P. N.; Baumberg, J. J.; Kelf, T. A.; Sugawara, Y.; Russell, A. E. *Faraday Discuss.* **2006**, *132*, 191−200.

(20) Mahajan, S.; Cole, R. M.; Soares, B. F.; Pelfrey, S. H.; Russell, A. E.; Baumberg, J. J.; Bartlett, P. N. *J. Phys. Chem. C* **2009**, *113*, 9284−9289.

(21) Tognalli, N. G.; Cortés, E.; Hernández-Nieves, A. D.; Carro, P.; Usaj, G.; Balseiro, C. A.; Vela, M. E.; Salvarezza, R. C.; Fainstein, A. *ACS Nano* **2011**, *5*, 5433−5443.

(22) Jose, B.; Mallon, C. T.; Forster, R. J.; Keyes, T. E. *Phys. Chem. Chem. Phys.* **2011**, *13*, 14705−14714.

(23) Scodeller, P.; Flexer, V.; Szamocki, R.; Calvo, E. J.; Tognalli, N. G.; Troiani, H.; Fainstein, A. *J. Am. Chem. Soc.* **2008**, *130*, 12690−12697.

(24) Tognalli, N. G.; Scodeller, P.; Flexer, V.; Szamocki, R.; Calvo, E. J.; Fainstein, A. *Phys. Chem. Chem. Phys.* **2009**, *11*, 7412−7423.

(25) Huang, F. M.; Wilding, D.; Speed, J. D.; Russell, A. E.; Bartlett, P. N.; Baumberg, J. J. *Nano Lett.* **2011**, *11*, 1221−1226.

(26) Mie, G. *Ann. Phys.* **1908**, *25*, 377−445.

(27) Le Ru, E. C.; Etchegoin, P. G. *Principles of surface enhanced Raman spectroscopy and related plasmonic effects*; Elsevier: Amsterdam, 2008.

(28) Abdelsalam, M. E.; Bartlett, P. N.; Russell, A. E.; Baumberg, J. J.; Calvo, E. J.; Tognalli, N. G.; Fainstein, A. *Langmuir* **2008**, *24*, 7018−7023.

(29) Mahajan, S.; Richardson, J.; Brown, T.; Bartlett, P. N. *J. Am. Chem. Soc.* **2008**, *130*, 15589−15601.

(30) Note that the reflectivity measurements, because of limitations of the ellipsometry setup, were taken at 25° and not at 15° as was the incidence angle set for the Raman experiments. This small difference has to be taken into account when comparing the experiments. We recall that Mie modes do not disperse with angle. Bragg modes, on the other hand, have small variations between 25° and 15° that, however, can be analytically corrected for.[14]

(31) Because of domain variations within a graded sample, the azimuthal angle was not controlled in these experiments. However, the $q_{\overline{11}}$ Bragg mode is the only PSPP mode that we have observed above the Au interband transition wavelength (∼600 nm), and it presents almost the same energy dispersion for both azimuthal angles, $\phi = 0°$ and $\phi = 30°$ according to ref 14.

(32) Orendoff, C. J.; Gearheart, L; Jane, N. R; Murphy, C. O. *Phys. Chem. Chem. Phys.* **2006**, *8*, 165−170.

(33) Kahl, M.; Voges, E. *Phys. Rev. B* **2000**, *61*, 14078−14088.